The Astrophysical Journal, 990:223, 2025, September 10
Typeset using LaTeX **twocolumn** style in AASTeX631
https://doi.org/10.3847/1538-4357/adf725

Analysis of vorticity production from irrotational turbulent collapse

ABSTRACT

1. INTRODUCTION

It is generally believed that gravitational collapse generates turbulence (Field et al. 2008; Klessen & Hennebelle 2010). While this is indeed quite plausible, it is unclear how well this can be demonstrated with numerical simulations today (Hennebelle 2021; Brandenburg & Ntormousi 2022, 2025). This question is particularly important in the context of small-scale dynamo action driven by the collapse, because it could result in an amplification of magnetic energy below the Jeans scale due to the collapse (Schober et al. 2026).

Small-scale dynamos operate predominantly due to vortical turbulence. On the other hand, gravitational collapse produces predominantly irrotational flows. The question of vorticity production from an irrotational collapse becomes particularly interesting when an isothermal equation of state is employed, because then vorticity production via the baroclinic term would be impossible. The only way to produce then vorticity from purely irrotational flows is via the interaction with viscosity.

Earlier work by Brandenburg & Ntormousi (2022, 2025) has already addressed this question and it was concluded that the collapse can enhance the magnetic field by compression, but this alone is not a dynamo. Nevertheless, dynamo action was found to occur, because it was due to the initial turbulence. This turbulence was decaying and not caused by the collapse itself. Distinguishing between these two mechanisms was facilitated by transforming the equations into a collapsing coordinate system (Brandenburg & Ntormousi 2025), which was based on a formalism first proposed by Muhammed Irshad et al. (2026).

An important step toward a demonstration of collapse-induced turbulence was based on a decomposition radial and transverse velocity components (Hennebelle 2021). Here, we focus on the basic question of vorticity production. To address this question, we employ a slightly supercritical Bonnor-Ebert geometry (Ebert 1955; Bonnor 1956) along with just irrotational velocity perturbations initially. No magnetic fields are included, because they would only obscure our basic question.

2. OUR MODEL

2.1. *Basic equations*

Following Schober et al. (2026), we work with a periodic domain of size $L^3 = (4\pi)^3$. A Bonnor-Ebert sphere of radius R is inserted at $|\boldsymbol{x}| = 0$, i.e., at the center of our domain. The sphere therefore repeats itself to infinity, but sufficiently far away from the periodic boundaries, the collapse resembles that of an isolated sphere.

We stress that we perform direct numerical simulations, so no subgrid scale modeling is done. Such modeling would modify the outcome the outcomes in ways that are difficult to interpret. In particular, the stress tensor must be strictly symmetric and is here given by $2\rho\nu\mathsf{S}$, where S is the traceless rate-of-strain tensor with the components $\mathsf{S}_{ij} = (\partial_i u_j + \partial_j u_i)/2 - \delta_{ij}\boldsymbol{\nabla}\cdot\boldsymbol{u}/3$. We assume an isothermal equation of state where the pressure is proportional to the density ρ and given by $\rho c_{\rm s}^2$, where $c_{\rm s}$ is the isothermal sound speed. Our equations are (Passot et al. 1995)

$$\nabla^2\Phi = 4\pi G\,(\rho - \rho_0)\,, \tag{1}$$

$$\frac{\mathrm{D}\boldsymbol{u}}{\mathrm{D}t} = -\boldsymbol{\nabla}\left(c_{\rm s}^2\ln\rho + \Phi\right) + \frac{1}{\rho}\boldsymbol{\nabla}\cdot(2\rho\nu\mathsf{S}), \tag{2}$$

$$\frac{\mathrm{D}\ln\rho}{\mathrm{D}t} = -\boldsymbol{\nabla}\cdot\boldsymbol{u}, \tag{3}$$

where Φ is the gravitational potential, G is Newton's constant, ρ_0 is the spatially averaged density, which is constant in time because of mass conservation, $\boldsymbol{u}$ is the velocity, and ν is the kinematic viscosity, which is here assumed to be constant.

2.2. *Initial velocity field*

We use the Pencil Code (Pencil Code Collaboration et al. 2021), which employs sixth-order centered differences and a third-order time-stepping scheme. We adopt a resolution of either 512^3 or 1024^3 mesh points. Here and below, angle brackets denote volume averaging.

Our initial velocity is constructed in Fourier space as $\boldsymbol{u}(\boldsymbol{x}) = \sum \tilde{\boldsymbol{u}}(\boldsymbol{k})\, e^{\mathrm{i}\boldsymbol{k}\cdot\boldsymbol{x}}$ with

$$\tilde{u}_i(\boldsymbol{k}) = \hat{k}_i\hat{k}_j\, u_{\rm ini}\tilde{S}_j(\boldsymbol{k}). \tag{4}$$

Here, $u_{\rm ini}$ is an amplitude factor, $\hat{k}_i$ are the components of the unit vector $\hat{\boldsymbol{k}} \equiv \boldsymbol{k}/k$, $\tilde{S}_j(\boldsymbol{k})$ is a vector field in

Fourier space with three independent components that depend on $k = |\boldsymbol{k}|$ but have random phases $\varphi(\boldsymbol{k})$ for each $\boldsymbol{k}$ vector. Here, we choose

$$\tilde{S}_j(\boldsymbol{k}) = \frac{k_0^{-3/2}(k/k_0)^{\alpha/2-1}}{1+(k/k_0)^{(\alpha+5/3)/2}}\, e^{(\mathrm{i}\varphi(\boldsymbol{k})-\boldsymbol{k}^2/k_{\rm cut}^2}, \quad (5)$$

where k_0 is the peak wavenumber of the initial condition, and α is the slope of the subinertial range, which we set to $\alpha = 4$ in this work.

2.3. *Vorticity Production*

To determine the terms leading to vorticity production, we take the curl of Equation (2) and find

$$\frac{\partial \boldsymbol{\omega}}{\partial t} = \boldsymbol{\nabla}\times\left[\boldsymbol{u}\times\boldsymbol{\omega} + \nu\left(\boldsymbol{G} - \boldsymbol{\nabla}\times\boldsymbol{\omega}\right)\right], \quad (6)$$

where $G_i = 2\mathsf{S}_{ij}\nabla_j \ln\rho$ is the crucial vector whose curl drives vorticity. The other two terms vanish initially, when there is no vorticity (Mee & Brandenburg 2006). Defining $\boldsymbol{q} = \boldsymbol{\nabla}\times\boldsymbol{\omega}$, and taking the dot product of Equation (6) with $\boldsymbol{\omega}$, we obtain after volume averaging and integration by parts

$$\frac{\mathrm{d}}{\mathrm{d}t}\left\langle \tfrac{1}{2}\boldsymbol{\omega}^2\right\rangle = \langle \boldsymbol{q}\cdot(\boldsymbol{u}\times\boldsymbol{\omega})\rangle + \nu\left(\langle \boldsymbol{q}\cdot\boldsymbol{G}\rangle - \langle \boldsymbol{q}^2\rangle\right). \quad (7)$$

Except for the term involving $\boldsymbol{G}$, this equation is analogous to the induction equation, where $\langle \boldsymbol{q}\cdot(\boldsymbol{u}\times\boldsymbol{\omega})\rangle$ is the term analogous to the magnetic energy generation by the induction term and $\nu\langle \boldsymbol{q}^2\rangle$ is analogous to the magnetic energy loss by the dissipation term. In this work, we monitor all three terms, along with the time derivative of the enstrophy, $\frac{1}{2}\langle\boldsymbol{\omega}^2\rangle$.

3. RESULTS

3.1. *Numerical constraints on the viscosity*

We recall that we perform direct numerical simulations, where dissipation is exclusively accomplished by the explicit viscosity, as quantified by the value of ν. We begin with a survey for different values of ν and also different number of meshpoints, N^3. In Figure 1, we show the time evolution of the Mach number, $\mathrm{Ma} = u_{\rm rms}/c_{\rm s}$, for different values of ν. We also show the nondimensional kinetic energy dissipation, $\epsilon_{\rm K}/c_{\rm s}^3 k_0$, as well as the time dependence of $\langle(\boldsymbol{\nabla}\cdot\boldsymbol{u})^2\rangle/c_{\rm s}^2k_0^2$ and $\langle(\boldsymbol{\nabla}\times\boldsymbol{u})^2\rangle/c_{\rm s}^2k_0^2$.

We see that the collapse occurs at a time between $t = 3$ and 3.2 with the lowest value of ν being the case with the earliest collapse. Until this time, all time traces are broadly similar, except that the more viscous runs display an early phase of more dissipation. This can be seen in the slightly lower values of the Mach number at $t = 0.5$ for the more viscous runs and the slightly larger

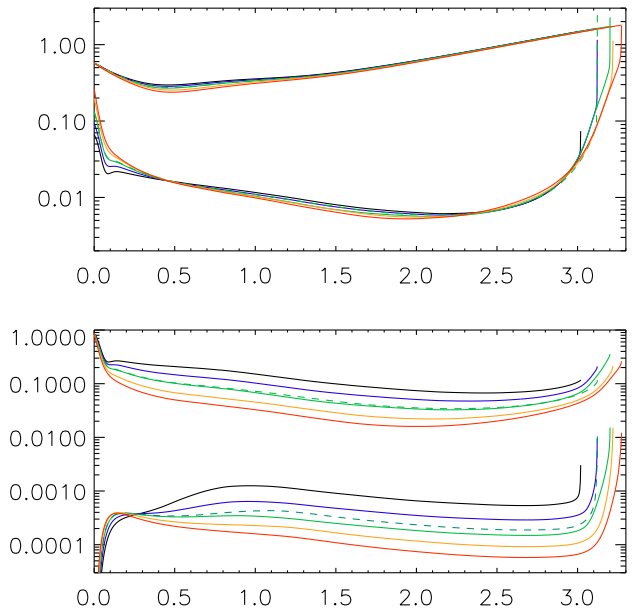

Figure 1. Time series of the Mach number, $\mathrm{Ma} = u_{\rm rms}/c_{\rm s}$, for different values of ν, along with the nondimensional kinetic energy dissipation, $\epsilon_{\rm K}/c_{\rm s}^3 k_0$, as well as the time dependence of $\langle(\boldsymbol{\nabla}\cdot\boldsymbol{u})^2\rangle/c_{\rm s}^2k_0^2$ and $\langle(\boldsymbol{\nabla}\times\boldsymbol{u})^2\rangle/c_{\rm s}^2k_0^2$.

dissipation before that time. The rms velocity starts to grow exponentially at the expected growth rate, which is insensitive to the value of ν. At the early phase of the exponential growth, the energy dissipation is less for the less viscous runs, but it becomes larger during the main phase of the collapse after $t = 2.5$. After $t = 2.8$, the runs may no longer be reliable at the present resolution.

During the early phase of the collapse at times before $t \approx 1.7$, both $\langle(\boldsymbol{\nabla}\cdot\boldsymbol{u})^2\rangle$ and $\langle(\boldsymbol{\nabla}\times\boldsymbol{u})^2\rangle \equiv \langle\boldsymbol{\omega}^2\rangle$ decay. Only the less viscous runs display a subsequent growth of $\langle(\boldsymbol{\nabla}\cdot\boldsymbol{u})^2\rangle$ after that time, while $\langle(\boldsymbol{\nabla}\times\boldsymbol{u})^2\rangle$ continues to decay all the way until $t \approx 2.7$, which is the time until we deem the runs reliable. It would be possible to go to higher numerical resolution, but the main point of our experiments was to reveal the severe limitation on the minimum viscosity that is needed for a reliable simulation.

A useful measure of the value of the viscosity is the mesh Reynolds number, $\mathrm{Re}_{\rm mesh} = u_{\rm rms}\delta x/\nu$, where $\delta x = L/N$ with $L = 4\pi$ is the size of the domain and δx is the mesh spacing. At $t = 2.8$, the time we deemed to be the limit beyond which we can trust the results, we find $\mathrm{Re}_{\rm mesh}$ to be between 0.7 and 1.5. Conversely, if we postulate the limit to be given by $\mathrm{Re}_{\rm mesh} = 0.7$, we would expect the 1024^3 run with $\nu = 0.02$ to be reliable until $t = 2.7$, and the run with 1024^3 run with $\nu = 0.01$ would only be reliable until $t = 1.9$; see .

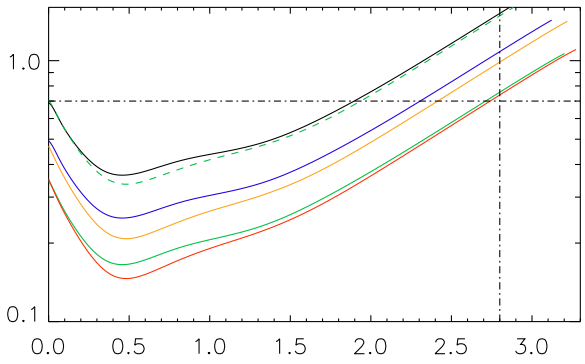

Figure 2. Mesh Reynolds number for all runs. The vertical dashed-dotted line marks the time $t = 2.8$ beyond which we deem the runs no longer trustworthy. while the horizontal dashed-dotted line marks the grid Reynolds number $\mathrm{Re}_{\mathrm{mesh}} = 0.7$ above which we also deem the runs no longer trustworthy.

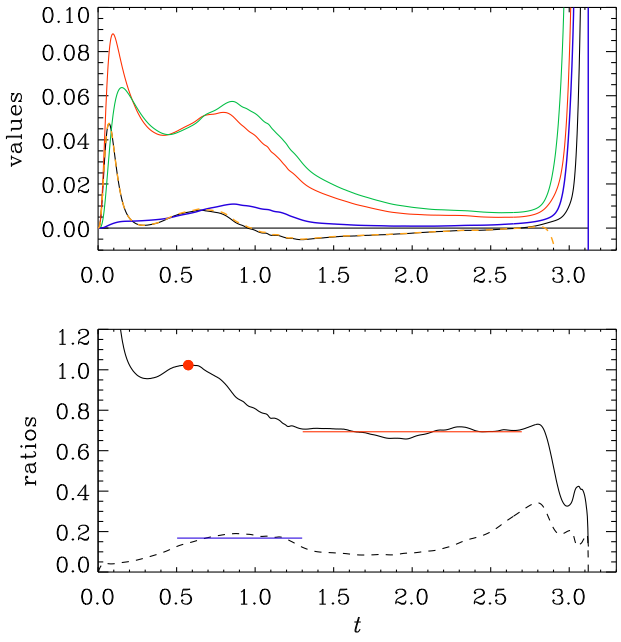

Figure 3. Top: $\langle \boldsymbol{q} \cdot (\boldsymbol{u} \times \boldsymbol{\omega}) \rangle$ (blue), $\nu \langle \boldsymbol{q} \cdot \boldsymbol{G} \rangle$ (red), and $\nu \langle \boldsymbol{q}^2 \rangle$ (green). The dashed orange line represents the combination of these three terms and the black line denotes the computed value of $\mathrm{d}\langle \frac{1}{2}\boldsymbol{\omega}^2 \rangle / \mathrm{d}t$. Bottom: ratio $\langle \boldsymbol{q} \cdot \boldsymbol{G} \rangle / \langle \boldsymbol{q}^2 \rangle$ (solid line) and $\langle \boldsymbol{q} \cdot (\boldsymbol{u} \times \boldsymbol{\omega}) \rangle / \nu \langle \boldsymbol{q}^2 \rangle$ (dashed line). The red filled symbol denotes the maximum of the first ratio after the initial transient before $t = 0.2$, the red line is the average of this ratio during the subsequent time interval from 1.3 to 2.7, and the blue line marks the average of the second ratio during the time interval from 0.5 to 1.3.

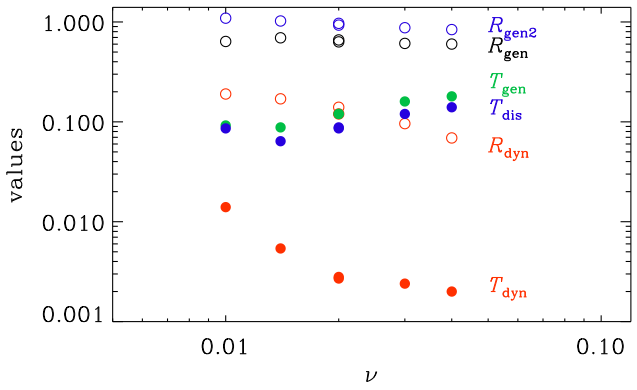

Figure 4. Scaling of the quantities ratm (R_{gen}), ratdm (R_{dyn}), genmax (T_{gen}), dismax (T_{dis}), and dynmax (T_{dyn}), with ν.

3.2. *Vorticity production terms*

We now analyze the three contributions to $\mathrm{d}\langle \frac{1}{2}\boldsymbol{\omega}^2 \rangle / \mathrm{d}t$ in Equation (7): $\langle \boldsymbol{q} \cdot (\boldsymbol{u} \times \boldsymbol{\omega}) \rangle$, $\nu \langle \boldsymbol{q} \cdot \boldsymbol{G} \rangle$, and $\nu \langle \boldsymbol{q}^2 \rangle$. The combination of all three contributions matches $\mathrm{d}\langle \frac{1}{2}\boldsymbol{\omega}^2 \rangle / \mathrm{d}t$ during the time when the run is reliable.

Each run is characterized by a very early adjustment phase ($t < 0.2$) when vorticity is being produced by the small departures from a perfectly irrotational flow. At the same time when vorticity is being produced, also $\nu \langle \boldsymbol{q}^2 \rangle$ begins to grow and almost tracks $\nu \langle \boldsymbol{q} \cdot \boldsymbol{G} \rangle$. The ratio $\langle \boldsymbol{q} \cdot \boldsymbol{G} \rangle / \langle \boldsymbol{q}^2 \rangle$ drops and reaches a second (but lower) maximum during the second early phase ($0.5 \leq t \leq 0.7$). and finally settles on an approximately constant value when this ratio is around 0.6; see Table 1 for an overview of these values for different runs. The dynamo-like term $\langle \boldsymbol{q} \cdot (\boldsymbol{u} \times \boldsymbol{\omega}) \rangle$ is always subdominant, and the ratio $\langle \boldsymbol{q} \cdot (\boldsymbol{u} \times \boldsymbol{\omega}) \rangle / \nu \langle \boldsymbol{q}^2 \rangle$ barely reaches 20%.

nu	ratm	ratdm	genmax	dismax	dynmax	run
1.0e-02	0.628	1.7e-01	9.2e-02	8.6e-02	1.4e-02	Hy1024b_noshock
1.4e-02	0.691	1.6e-01	8.8e-02	6.4e-02	5.4e-03	Hy1024c_noshock
2.0e-02	0.657	1.2e-01	1.2e-01	8.6e-02	2.7e-03	Hy1024a_noshock
2.0e-02	0.629	1.4e-01	1.2e-01	8.8e-02	5.9e-03	Hy512d_noshock
3.0e-02	0.604	9.6e-02	1.6e-01	1.2e-01	2.4e-03	Hy512e_noshock
4.0e-02	0.596	7.0e-02	1.8e-01	1.4e-01	2.0e-03	Hy512g_noshock

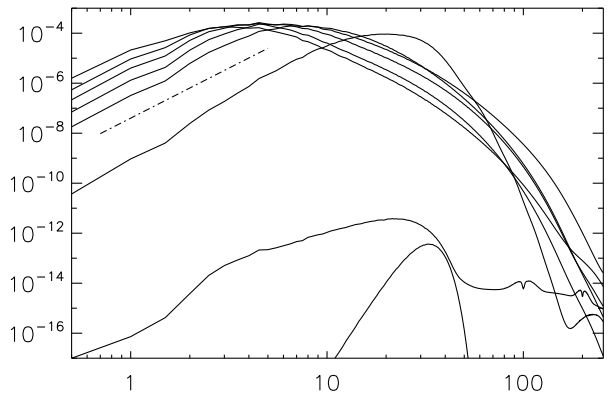

Figure 5. Vorticity spectrum for 2e-2. Note the k^4 subinertial range spectrum in $\boldsymbol{\omega}$, in close analogy to a similar behavior of $\boldsymbol{B}$ in MHD. As elsewhere, we have $k_0 = 5 \times 0.5 = 2.5$ and $k_{\rm cut} = 50 \times 0.5 = 25$ (the default is `lscale_tobox=T`, and $k_1 = 0.5$).

3.3. *Vorticity spectra*

Let us now inspect the scale dependence of vorticity. For that purpose, we plot spectra of $\boldsymbol{\omega}$ at different times; see Figure 5. Very quickly, a vorticity spectrum builds up with a peak at $k \approx 30$. Once a forward spectrum of vorticity has been generated, we also see the growth of spectral vorticity at the lowest wavenumber, which is akin of the inverse cascade found previously for magnetic field. This finding suggests a more detailed analogy between vorticity and the magnetic field in MHD, which goes beyond just the mathematical similarity between the two equations. An important difference is of course the existence of the generation term, $T_{\rm gen}$.

REFERENCES

Bonnor, W. B. 1956, MNRAS, 116, 351, doi: 10.1093/mnras/116.3.351

Brandenburg, A., & Ntormousi, E. 2022, MNRAS, 513, 2136, doi: 10.1093/mnras/stac982

—. 2025, ApJ, 990, 223, doi: 10.3847/1538-4357/adf725

Ebert, R. 1955, ZA, 37, 217

Field, G. B., Blackman, E. G., & Keto, E. R. 2008, MNRAS, 385, 181, doi: 10.1111/j.1365-2966.2007.12609.x

Hennebelle, P. 2021, A&A, 655, A3, doi: 10.1051/0004-6361/202141650

Klessen, R. S., & Hennebelle, P. 2010, A&A, 520, A17, doi: 10.1051/0004-6361/200913780

Mee, A. J., & Brandenburg, A. 2006, MNRAS, 370, 415, doi: 10.1111/j.1365-2966.2006.10476.x

Muhammed Irshad, P., Bhat, P., Subramanian, K., & Shukurov, A. 2026, PhRvL, 136, 091201, doi: 10.1103/fp1v-xrr5

Passot, T., Vazquez-Semadeni, E., & Pouquet, A. 1995, ApJ, 455, 536, doi: 10.1086/176603

Pencil Code Collaboration, Brandenburg, A., Johansen, A., et al. 2021, JOSS, 6, 2807, doi: 10.21105/joss.02807

Schober, J., Abramson, M., Mandal, S., Mtchedlidze, S., & Kahniashvili, T. 2026, arXiv e-prints, arXiv:2602.23263, doi: 10.48550/arXiv.2602.23263